# Journal Pre-proof

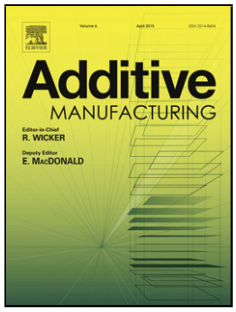


Combined effect of surface anomalies and volumetric defects on fatigue assessment of AlSi7Mg fabricated via laser powder bed fusion

Milad Hamidi Nasab, Simone Romano, Dario Gastaldi, Stefano Beretta, Maurizio Vedani

PII: S2214-8604(19)31099-1

DOI: https://doi.org/10.1016/j.addma.2019.100918

Reference: ADDMA 100918

To appear in: *Additive Manufacturing*

Received Date: 23 July 2019

Revised Date: 20 September 2019

Accepted Date: 14 October 2019

Please cite this article as: Hamidi Nasab M, Romano S, Gastaldi D, Beretta S, Vedani M, Combined effect of surface anomalies and volumetric defects on fatigue assessment of AlSi7Mg fabricated via laser powder bed fusion, *Additive Manufacturing* (2019), doi: https://doi.org/10.1016/j.addma.2019.100918

# Combined effect of surface anomalies and volumetric defects on fatigue assessment of AlSi7Mg fabricated via laser powder bed fusion

**Milad Hamidi Nasab*[1], Simone Romano[1], Dario Gastaldi[2], Stefano Beretta[1], Maurizio Vedani[1]**

1. *Department of Mechanical Engineering, Politecnico di Milano, Italy*
2. *Department of Chemistry, Materials and Chemical Engineering, Politecnico di Milano, Italy*

*Corresponding author.
E-mail address: Milad.hamidi@polimi.it
Postal address: Via. Giuseppe La Masa 1 (Dipartimento Meccanica), 20156, Milano (IT)

**Abstract**

In recent years, the fabrication of aluminum alloy parts via laser powder bed fusion has been extensively considered in the biomedical, aerospace, and other industrial sectors, as it provides advantages such as the ability to manufacture complex shapes with high performance associated with lightweight design. However, surface irregularities and sub-surface defects limit the full exploitation of such parts in fatigue-critical applications. Moreover, most of the commonly used metrological methods for surface characterization have proven to be unsuitable for determining important features such as undercuts and sub-surfaces pores. Hence, a comprehensive coupled investigation of metrological methods and cross-sectional analysis were performed in this study to evaluate the effects of surface features and volumetric defects typical of additively manufactured materials. Fatigue tests and fractographic analyses were conducted to support the finite element simulations and proposed fracture mechanics model. The results demonstrate that the standard metrological methods cannot provide all of the data needed to model the fatigue behaviors of additively manufactured materials robustly. Moreover, a statistical model describing the competition between volumetric defects and surface irregularities was developed and validated.

**Keywords:** additive manufacturing, fracture mechanics, laser powder bed fusion, metrological method, surface morphology, defects

**Nomenclature**

| | |
|---|---|
| $E_L$ | contour line energy |
| $P_L$ | laser power |
| $t_s$ | exposure time |
| $P_d$ | point distance |
| $T_L$ | powder layer thickness |
| $D_h$ | hatch distance |
| $r_0$ | spot size |
| $R$ | load ratio |
| $Ra$ | arithmetical mean roughness value |
| $RPc$ | peak count |
| $RSm$ | mean peak width |
| $Sa$ | arithmetical mean height of the S-L surface |
| $Spd$ | peak density |
| $Ssk$ | skewness |
| $\lambda$ | scale parameter |
| $\delta$ | shape parameter |
| $K$ | stress intensity factor |
| $\sigma$ | applied stress |

| | |
|---|---|
| $a$ | crack depth |
| $Y$ | boundary correction factor |
| $E$ | young's modulus |
| $v$ | poisson's ratio |
| $a^*$ | effective crack size |
| $w$ | width of the contour layer |
| $l_{90}$ | critical surface length subjected to at least 90% of the maximum applied stress |
| $l_0$ | reference surface length |
| $V_{90}$ | critical volume subjected to at least 90% of the maximum applied stress |
| $F$ | cumulative distribution function |
| $\sqrt{\text{area}}_{\text{SF}}$ | maximum defect size corresponding to surface features |
| $\sqrt{\text{area}}_{\text{VD}}$ | maximum defect size corresponding to volumetric defects |
| $F_{\text{SF}}$ | cumulative distribution function of the maximum surface feature size |
| $f_{\text{VD}}$ | probability density function of the experimental VD size distribution |

*Acronyms*

| | |
|---|---|
| cdf | cumulative distribution function |
| AM | additive manufacturing |
| AMZ | altered material zone |
| BCF | boundary correction factor |
| CAD | computer-aided design |
| FCG | fatigue crack growth |
| FE | finite element |
| LEVD | largest extreme value distribution |
| LoF | lack of fusion |
| L-PBF | laser-based powder bed fusion |
| µCT | X-ray micro-computed tomography |
| NA | numerical aperture |
| OM | optical microscope |
| SEM | scanning electron microscope |

## 1. Introduction

Additive manufacturing (AM) technologies enable the production of structural and functional parts via layer-by-layer addition of material, starting from 3D digital computer-aided designs (CADs). Among the various techniques available, laser powder bed fusion (L-PBF) is the most common technique utilized for printing nearly net-shaped metallic parts from the base metallic powder. L-PBF has received extensive attention in the past few years for the production of complex geometries, customized parts, and open cell structures (3D lattices) with little material waste for the aerospace, biomedical, and automotive industries [1–4].

Many previous studies have been focused on optimization of the processing or post-processing techniques such as heat treatment and surface finishing of the as-built parts due to their poor surface quality compared to conventionally manufactured parts [5–16]. Surfaces produced by L-PBF suffer from high roughness and irregularities due to the layer-by-layer nature of the building process and the presence of particular contaminants, such as spatter, balling, and partially melted metal powder [17–24]. Furthermore, the presence of the so-called altered material zone (AMZ), corresponding to the sub-surface layers of parts whose properties differ from those of the bulk material due to the use of different contour process

parameters also requires thorough assessment [5,25]. The aforementioned surface and sub-surface anomalies could cause additional notch effects and trigger fatigue crack initiation, thereby affecting the performance of the parts [26,27]. Therefore, a compatible approach to surface metrology is urgently necessary to understand the quality of manufactured parts. AM surfaces have freeform geometry and are combinations of structured surface textures with random features, which makes them very difficult to analyze using conventional metrological methods [28,29].

Numerous reports have been published on the surface metrology of additive manufactured parts based on roughness evaluation using stylus profilometers [6,18,24,30–35] and other non-contact methods such as confocal microscopy [36–38], focus variation microscopy [31], coherence scanning interferometry [39,40] and X-ray micro-computed tomography (μCT) [41–47]. However, a combined study of the surfaces of AM materials using metrological methods and cross-sectional analysis aimed at coupling the surface roughness parameters with the features of the AMZ has not yet been performed. Among the various aspects affected by the surface quality, one of the most complex and widely debated is the fatigue strength. In fact, the fatigue properties of net-shaped AM parts are largely affected by the previously described surface features (SFs) and flaws [48]. Considering parts with machined or high-quality surfaces, fatigue strength is mostly driven by volumetric defects (VDs) falling in the surface or sub-surface regions [49,50]. In these cases, several authors have shown that defects can be treated in the form of short cracks by describing their size using the $\sqrt{\text{area}}$ parameter proposed by Murakami [51]. The effects of such defects on the fatigue strength can be assessed by using the Kitagawa-Takahashi diagram [45,48,52–54] or performing fatigue crack growth simulations [50,55,56]. In contrast, the effects of the typical SFs caused by AM are currently being debated and no standardized methods of robustly determining the effects of the surface on fatigue performance are available.

Two primary approaches have been adopted in previous work to consider the effects of net-shape surface conditions: (i) evaluation of the stress concentration induced by SFs [46,53,57–59] and (ii) estimation of the empirical [53,60–62] or fictitious (i.e., equivalent initial flaw size approach) [63–65] size of the SFs and application of fracture mechanics concepts [65].

As fatigue phenomena are driven by the largest and most detrimental features present in the most loaded volume, the ability to measure or estimate the size of the most detrimental feature is essential to perform fatigue assessment of parts fabricated via AM correctly [66]. Thus, fatigue strength must be evaluated as a “competing” risk between the VDs and SFs. In this paper, a new approach is proposed whereby both VDs and SFs are treated as short cracks and their criticality is evaluated via fracture mechanics approaches, by describing their sizes using the $\sqrt{\text{area}}$ parameter.

The present report describes the experimental investigation and modeling performed to evaluate the effects of the surface quality of AM materials on the fatigue strength. For this purpose, various metrology methods and fracture mechanics modeling were considered to select the most significant parameter determining the fatigue properties of the investigated material. Based on this approach, a probabilistic model usable for estimating the critical failure mechanism by competing-risk assessment of the VDs and SFs of AM parts was developed. The model was finally validated by performing fatigue tests on AlSi7Mg samples produced by L-PBF, according to various process conditions.

## 2. Materials and methods

### *2.1. Material and sample manufacturing*

All of the samples in this study were manufactured via L-PBF by utilizing a Renishaw AM250 system (Wotton-under-Edge, UK) with a single-mode pulsed fiber laser with a maximum power of 200 W, focused to a spot size of 75 µm. The powder adopted was a commercial gas atomized AlSi7Mg (A357) alloy supplied by LPW Technology Ltd. (Runcorn, UK), whose chemical composition is reported in **Table 1**. The alloy belongs to the Al-Si-Mg alloy system, which is widely used for L-PBF processing.

| Si | Mg | Mn | Fe | Ti | Zn | Cu | Al |
|---|---|---|---|---|---|---|---|
| 6.7 – 7.3 | 0.25 – 0.45 | 0.5 – 0.6 | 0.14 | 0.08 – 0.12 | 0.09 | 0.04 | bal. |

**Table 1.** Chemical composition of the AlSi7Mg alloy powder (wt. %).

Cubic specimens with dimensions of 20 mm × 20 mm × 20 mm were printed on the 250 mm × 250 mm wide build envelope in a circular distribution, with equal radial distance and orientation from the axis of the laser source to avoid the effects of position dependency on the printed parts. All of the samples were printed with identical core process parameters and different contour line process parameters to generate different SFs and promote various sub-surface defects mainly located at the contour–core interface regions. The energy input of a single scan vector (e.g., contour line energy $E_L$) can be calculated from the ratio between the product of the laser power ($P_L$) and exposure time ($t_S$) and the point distance ($P_d$), according to Eq. (1):

$$E_L = \frac{P_L.t_S}{P_d}. \quad (1)$$

| $P_L$ (W) | $t_s$ (µs) | $P_d$ (µm) | $T_L$(µm) | $D_h$(µm) | $r_0$ (µm) |
|---|---|---|---|---|---|
| 200 | 140 | 80 | 25 | 100 | 75 |

**Table 2.** Core process parameters used in the building of the AlSi7Mg samples.

| Surface code | $P_L$ (W) | $t_s$ (µs) | $P_d$ (µm) | $E_L$ (J/m) |
|---|---|---|---|---|
| **S01** | 200 | 140 | 80 | 350 |
| **S02** | 150 | 140 | 80 | 263 |
| **S03** | 200 | 85 | 75 | 226 |
| **S04** | 150 | 85 | 75 | 169 |
| **S05** | 150 | 42 | 50 | 125 |
| **S06** | 100 | 85 | 75 | 113 |
| **S07** | 100 | 42 | 50 | 83 |

**Table 3.** Contour line process parameters used in the building of the AlSi7Mg samples. The contour-hatch spacing stays the same in all the cases being equal to 70 µm.

The process parameters of the core and contour line used to manufacture the cubes are presented in **Tables 2** and **3** respectively, where $T_L$, $D_h$, and $r_0$ are the powder layer thickness, hatch distance, and spot size, respectively. Considering the hatch distance and spot size data given in **Table 2**, significant overlapping of the tracks is expected. Relatively large overlapping of the tracks (both laterally and depth-wise) is desirable to improve the homogeneity of the structure and circumvent defects related to lack of fusion at the track edges. Various line energies were chosen to tailor distinct SFs in the interest of better outlining the effects of the surface irregularities on the fatigue behavior of the AlSi7Mg alloy obtained by L-PBF.

### *2.2. Metrology and texture analysis of the surfaces*

Two metrological methods were employed for the side vertical surfaces to distinguish the effects of each measurement method on the acquired data and calculated surface parameters. Contact-based measurements were performed using a Mahr-Perthometer PGK 120 profilometer with a MFW-250 90°/2 µm probe and a Gaussian filter, in accordance with the ISO 4288:1996 standard [67]. The measurement distance was set to 5.6 mm, and an 0.8 mm cut-off filter was employed. Five measurements for each sample

were performed to calculate the average value and standard deviation of the data. Subsequently, non-contact-based measurements were performed using an Olympus LEXT OLS4100 confocal microscope with a lateral resolution of 0.12 µm and a vertical resolution of 10 nm. The specimens were measured with a 10 × 0.3 numerical aperture objective and a 2.9 mm × 2.9 mm areal test field. Nine acquisitions, each with dimensions of 1 mm × 1 mm, were collected for each sample and stitched together with 5% overlap. Before calculating any surface parameters, the three-axis raw data were subjected to a linear form removal, followed by spatial filtering (median denoising 5 × 5) to remove spurious points. Subsequently, a Gaussian convolution F-filter with a 2.9 mm cut-off was applied equally to the length of the test field to eliminate the waviness at scales larger than the field of view, producing S-F surfaces. Next, another Gaussian convolution L-filter with a 0.8 mm cut-off was applied to circumvent smaller scale waviness, yielding S-L surfaces. These cut-off values were selected based on visual inspection of the analyzed surfaces and are in agreement with those reported in previous literature [36]. The data were then processed using MountainMap 7 software to obtain surface parameters based on the ISO 25178-2 standard [68].

*2.3 Metallographic analyses*

Images of the alloy microstructure were obtained from samples sectioned along planes parallel to the build direction (z direction) after grinding, polishing, and etching using Keller's reagent. The metallographic sample preparation was accurately carried out in order to avoid smearing of pores and other surface features. Analyses were conducted using a Zeiss EVO 50 EP scanning electron microscope (SEM) and a Nikon Eclipse LV150NL optical microscope (OM) for a detailed evaluation of the surface and sub-surface defects. Particular attention was paid to the microstructure along the regions intersecting the surface profiles and just beneath them, in the AMZ regions.

*2.4. Fatigue testing*

Based on the analyses of the seven conditions investigated (see Table 3), three sets of surfaces characterized using different morphological features were selected to evaluate the fatigue performance as a function of the surface properties (S01, S05, and S07).

Nine three-point bending fatigue samples per condition were then fabricated using the same parameters as those listed above and according to the design depicted in **Fig. 1**. These samples were printed horizontally with the surface of interest being the side vertical surface. The sample thickness was set to 5 mm. The design proposed by Boniotti et al. [69] was employed for these small samples, with the objective of accelerating the tests and reducing the experimental effort for evaluating the effects of the as-built surface on the fatigue properties. The as-built samples were then subjected to direct aging at 160 °C for 4 h (T5 heat treatment) [70].

Three-point bending fatigue tests in the load-controlled mode were performed using an MTS Acuman 3 electrodynamic test system with a loading capacity of up to 3 kN. The fatigue tests were performed on the three sets of samples with a load ratio *R* of 0.1 in an ambient temperature environment, at constant stress ranges with a maximum applied stress varying from 140 to 220 MPa to investigate fatigue lives between $5\times10^4$ cycles and the runout limit, which was set to $5\times10^6$ cycles. The test frequency was set to 30 Hz.

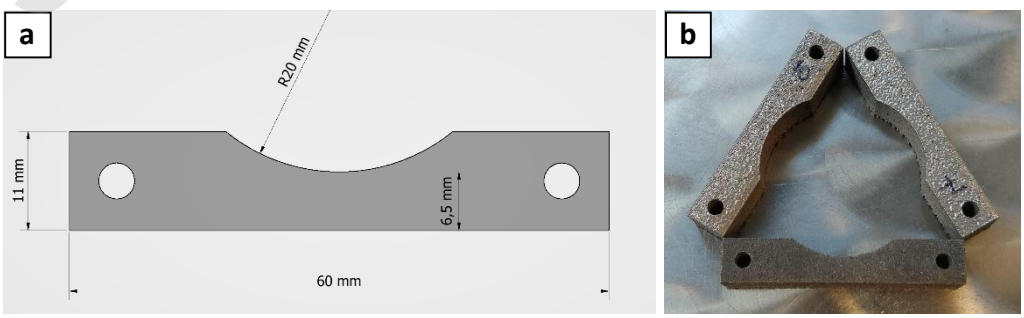

**Fig. 1.** Geometry of the three-point bending fatigue samples printed via L-PBF using AlSi7Mg powders: (a) sample geometry; (b) printed fatigue samples with different surface conditions.

*2.5 Fractographic analyses*

The fracture surfaces of all of the broken fatigue samples were analyzed using the SEM to identify the nucleation site and extent of the crack growth region and to perform statistical analyses on their extents. After identifying the nucleation site, the area of the defect responsible for the failure was measured using the image analysis software ImageJ, to obtain the distribution of the critical defect size in terms of the $\sqrt{\text{area}}$ parameter proposed by Murakami, which considers the defect area projected onto a plane perpendicular to the applied stress [51].

**3. Results**

*3.1. Morphology of surfaces*

Representative SEM images for a selection of three of the investigated surfaces (S01, S05, and S07) are presented in **Fig. 2**. The S01 specimen, with highest line energy ($E_L$ = 350 J/m), shows a fairly smooth surface, occasionally covered with typical L-PBF SFs such as spatter, partially unmelted metal powder, and balling (**Fig. 2a**). The formation mechanisms of these features are explained elsewhere [17]. In comparison, the S07 specimen (**Fig. 2c**), featuring the lowest line energy ($E_L$ = 83 J/m), clearly shows a greater density of the abovementioned SFs, although the average size of the spatter decreases significantly. Careful observation of the S05 and S07 samples (**Figs. 2b** and **2c,** respectively) also reveals the presence of pores (indicated by the arrows in **Fig. 2**). These two effects moving from higher to lower line energies were consistent in all of the printed specimens and are attributable to the insufficient energy densities, resulting in breakdown of the already solidifying melt pool (i.e., balling effect) and creating porous surfaces [21,22,71,72].

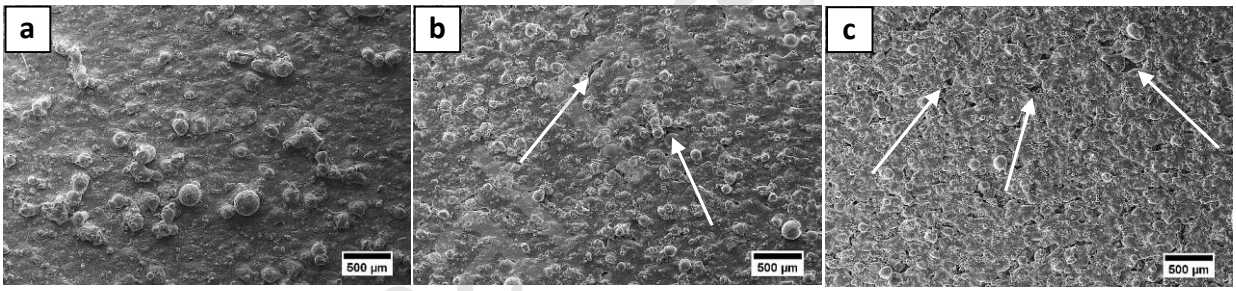


**Fig. 2.** SEM images of the lateral surfaces (parallel to the building direction) of the cubes printed under different contour line energies by L-PBF: (a) S01 $E_L$ = 350 J/m, (b) S05 $E_L$ = 125 J/m, and (c) S07 $E_L$ = 83 J/m.

*3.2. Comparison of surface topographies*

The typical characteristics of the surfaces generated via L-PBF were measured according to the ISO 4288:1996 [67] standard, and the surface parameters were calculated based on data collected using the contact-based profilometer, as presented in **Fig. 3a**. Four surface parameters were considered [24]: the arithmetic mean roughness (*Ra*), peak count (*RPc*), mean peak width (*RSm*), and maximum valley depth (*Rv*).

Four areal surface parameters based on ISO 25178-2 [68] were also evaluated (**Fig. 3b**): the arithmetical mean height of the S-L surface (*Sa*), peak density (*Spd*), skewness (*Ssk*), and maximum valley depth (*Sv*). Amongst these parameters, *Ssk* is known to be the most sensitive due to the presence of outliers in the data [73], as its calculation involves summation of the third power of surface height values [36]. This unitless parameter can be positive, negative, or zero and describes the shape of the topography height distribution. A surface with a random (or Gaussian) height distribution that has symmetrical topography has a skewness of zero. Furthermore, a surface with the bulk material below the mean line (indicating the presence of no pores on the surface) has a positive skewness, while a surface with the bulk material above the mean line (indicating the presence of deep valleys) has a negative skewness [73].

The trend of the *Ra* values in **Fig. 3a** shows an 80% increase when moving from S07 ($E_L$ = 83 J/m) to S01 ($E_L$ = 350 J/m). As presented in **Fig. 3b**, *Sa* does not show the same sensitivity as *Ra* to the line energy parameter, which is attributable to the effect of the probe size and shape limitations in contact-based roughness measurement. In this method, the stylus may interact with the steep sides of surface asperities, causing irregularity and temporary loss of contact [19]. Additionally, *Rv* and *Sv* show higher inconsistency in the trend and size of the recorded valley depth. However, *RPc* and *Spd* agree with each other, both showing a decrease in the number of peaks at higher line energies.

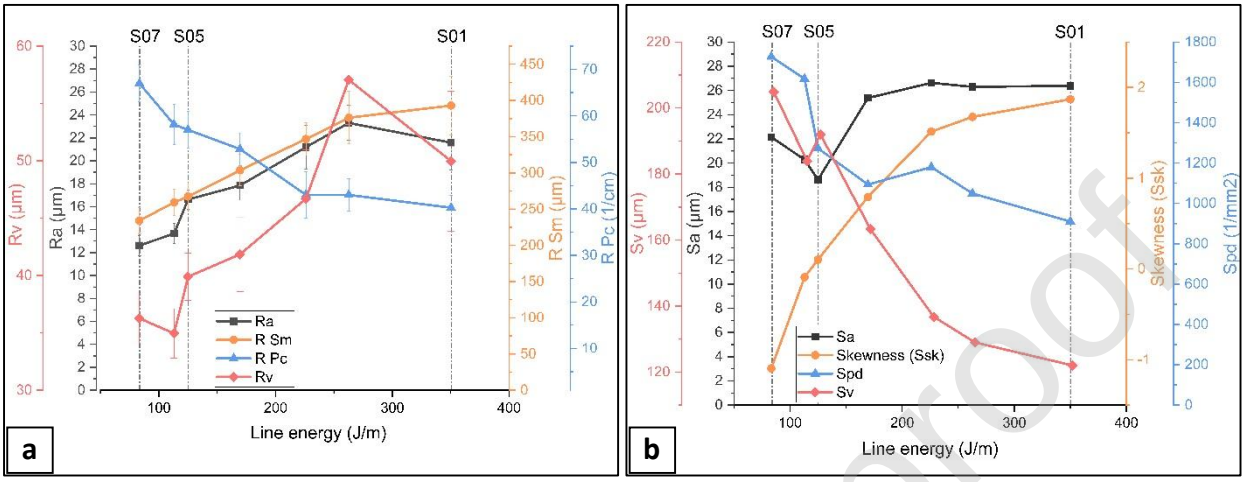


**Fig. 3.** Surface parameters measured by (a) contact-based profilometer and (b) confocal microscopy.

**Fig. 4** depicts the areal surface topographies acquired by confocal microscopy. Analysis of the data in **Fig. 3** reveals that the surfaces printed with low contour line energies (S05 and S07) exhibit high peak densities (*Rpc*) accompanied by low-width (*RSm*) peaks. These tendencies are also illustrated in **Figs. 2** and **4**, which reveal more SFs with smaller size for surfaces printed with lower line energies (i.e., S05 and S07) compared to the surface printed with higher line energy (i.e., S01). Consistently, the S07 specimen shows negative skewness (*Ssk*) expressed as the negative bias in the downward direction in the amplitude distribution (supported by the extensive numbers of superficial pores in **Figs. 2c** and **4c**), while the S01 specimen shows a high positive skewness attributable to its bulky surface and the presence of large particles on the surface, which produce a positive bias in the upward direction of the amplitude distribution. The S05 specimen shows a value very close to zero, which would be described as a random (or Gaussian) height distribution [73]. The *Sv* values are consistent with the skewness values as they represent the maximum depth of the valleys, with a deepest valley of 205 µm for S07 (having a negative skewness) and a lowest valley depth of 122 µm for S01 (having a positive skewness).

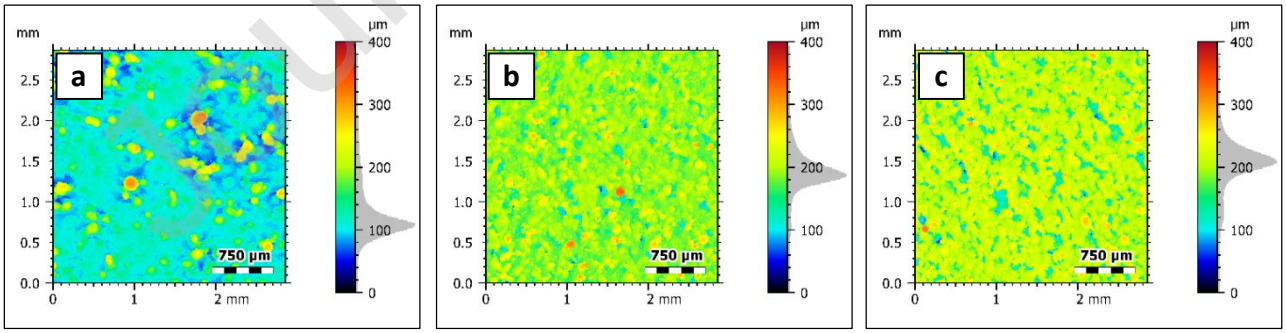


**Fig. 4.** Topographies of cubic specimens measured by confocal microscopy: (a) S01 $E_L$ = 350 J/m, (b) S05 $E_L$ = 125 J/m, and (c) S07 $E_L$ = 83 J/m.

*3.3. Surface profile analysis*

The surface profiles were investigated by analyzing the polished sections of the samples to achieve a wide overview of the surface and sub-surface features created by the L-PBF process. As expected based on the results of the topological examinations, **Fig. 5** confirms the presence of very diverse SFs for the three surface conditions investigated. The S01 specimen (**Fig. 5a**) is characterized by a bulky surface with occasional stuck coarse particles corresponding to spatter. This characteristic is attributable to a contour line energy sufficiently large to avoid balling and undercutting. On the contrary, the S05 and S07 specimens (**Figs. 5b** and **5c**) exhibit porous surfaces due to the lower contour line energy provided. The presence of the AMZ seems to be intensified for lower line energies, resulting in an interconnected undercut structure beneath the nominal contour line. It should be noted that this detailed information about these features could not be provided by either a stylus profilometer or confocal microscopy due to the intrinsic nature of these methods.

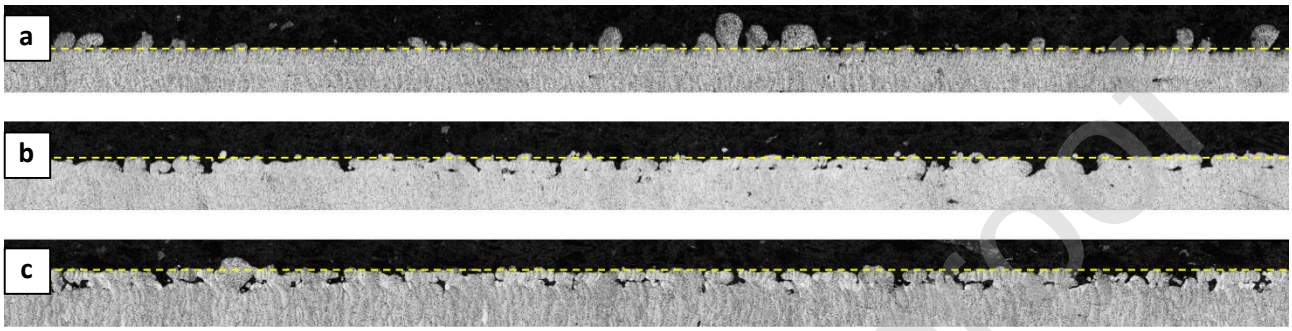


**Fig. 5.** Transverse sections of the cubic specimens taken by the OM: (a) S01 $E_L$ = 350 J/m, (b) S05 $E_L$ = 125 J/m, and (c) S07 $E_L$ = 83 J/m. The profile length is 20 mm, and the build direction is horizontal. The position of the ideal average surface lines is represented by the dashed yellow lines.

According to fracture mechanics, the criticality of a surface can be estimated by measuring the size of the deepest AMZ features. Similarly to the method suggested by the ASTM E2283 standard for evaluating inclusions on polished sections [74], the defect size was identified by dividing the 20 mm length of the polished surfaces into 20 subunits of 1 mm length each and performing *block maxima* sampling. This extreme-value sampling method consists of measuring the greatest depth of intrusions detected in each subunit region starting from an ideal average surface line tangent to the outer profile and corresponding to the ideal position of the surface, as defined in the CAD and depicted in **Fig. 5**. According to this procedure, 20 measurements per condition were obtained, describing the distribution of the maximum feature depth over a 1 mm surface length. The 20 maximum data for each surface condition were then described using a *largest extreme value distribution* (LEVD). The cumulative distribution function (cdf) of the LEVD is mathematically given by

$$F(x) = \exp\left(-\exp\left(-\frac{x-\lambda}{\delta}\right)\right), \quad (2)$$

where $\lambda$ and $\delta$ are the scale and shape parameters of the distribution, respectively. The three LEVDs obtained are depicted in the probability plot of **Fig. 6**, where the *y*-axis reports the reduced variable $-\log(-\log(F))$ (explained in [74]).

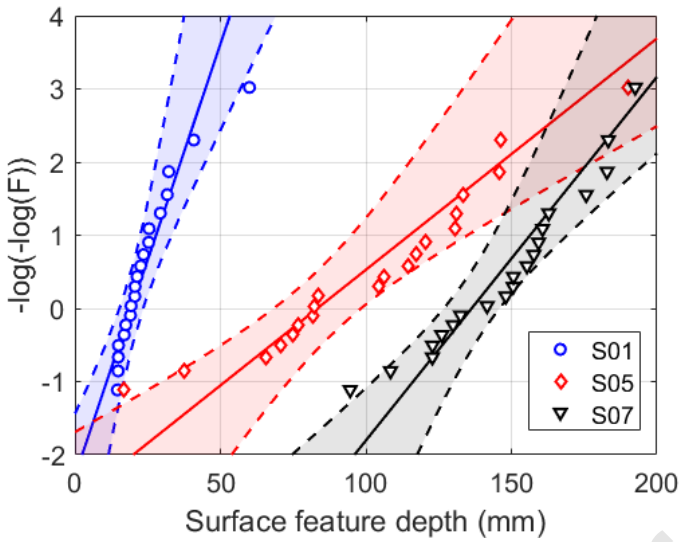


**Fig. 6.** Comparison of LEVDs of maximum SF depth for the three surface conditions.

**Table 4** summarizes the results obtained for the three surface conditions investigated. The measurements apparently contradict the results obtained by surface roughness analysis based on the average values, as S01 appears to have the best surface conditions, while S07 is expected to have the worst conditions considering this parameter. Conversely, *Sv* confirms the measurements performed on the polished sections. Even if the surface conditions of S05 look completely different from those of S07, similar depth values were recorded, with S05 characterized by a slightly smaller average defect depth but larger standard deviation.

| Surface code | Maximum depth (mm) | Average depth (mm) | Standard deviation (mm) | *Sv* (mm) |
|---|---|---|---|---|
| **S01** | 0.060 | 0.024 | 0.011 | 0.112 |
| **S05** | 0.190 | 0.102 | 0.041 | 0.190 |
| **S07** | 0.193 | 0.148 | 0.026 | 0.205 |

**Table 4.** Summary of the SF depths measured on the polished sections and *Sv* obtained by confocal microscopy.

*3.4. Fatigue testing results*

The results of the three-point bending fatigue tests are presented in **Fig. 7**. The tests were found to be fairly repeatable and characterized by limited scattering effects. Greater variability was obtained at the lowest stress level, which demonstrates the proximity of the fatigue limit. Surprisingly, no significant variations in the Wöhler curve position were detected among the three sets of specimens despite the important differences detected in terms of surface conditions, as described in Section 3.3.

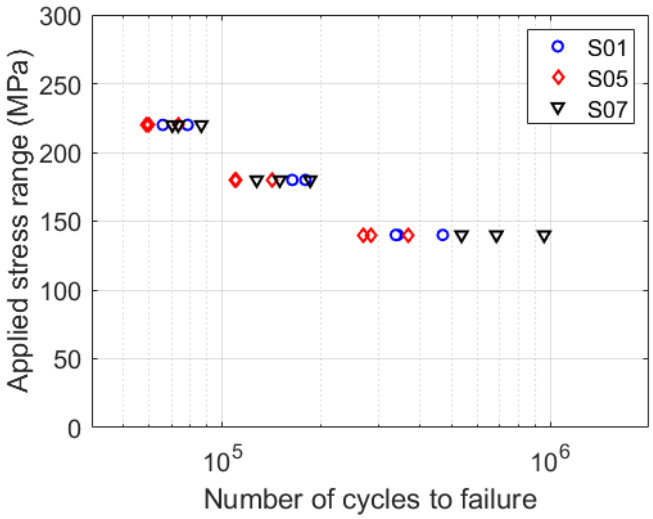


**Fig. 7.** Results of high-cycle fatigue tests.

*3.5. Investigation of fracture surfaces*

Post-mortem fractographic analyses showed that all of the specimens failed due to defects nucleated on the surface. Careful analysis of the fracture surfaces enabled us to distinguish two different types of flaws causing failure: (i) VDs caused by occasional lack of fusion (LoF) porosity and (ii) other SFs. Despite the apparent similarity of the fatigue results, the nucleation mechanism (i.e., the frequencies of the two defect types) proved to be very different in the three batches of samples.

In the S01 samples, all of the failures originated from VDs (see the two examples in **Fig. 8**). As expected, the LoF defects are aligned along the powder layer plane. In the S05 samples, the failures were caused by both volumetric LoF and surface-related features (**Fig. 9**) with almost equal probability. **Figs. 9a** and **9b** depict failure due to LoF (VD), while **Figs. 9c** and **9d** show the presence of a sub-surface cavity due to incomplete wetting between the contour layer and material core as a result of the presence of large spatter particles on the surface. Finally, the S07 samples failed mostly due to SFs (**Figs. 10c** and **10d**).

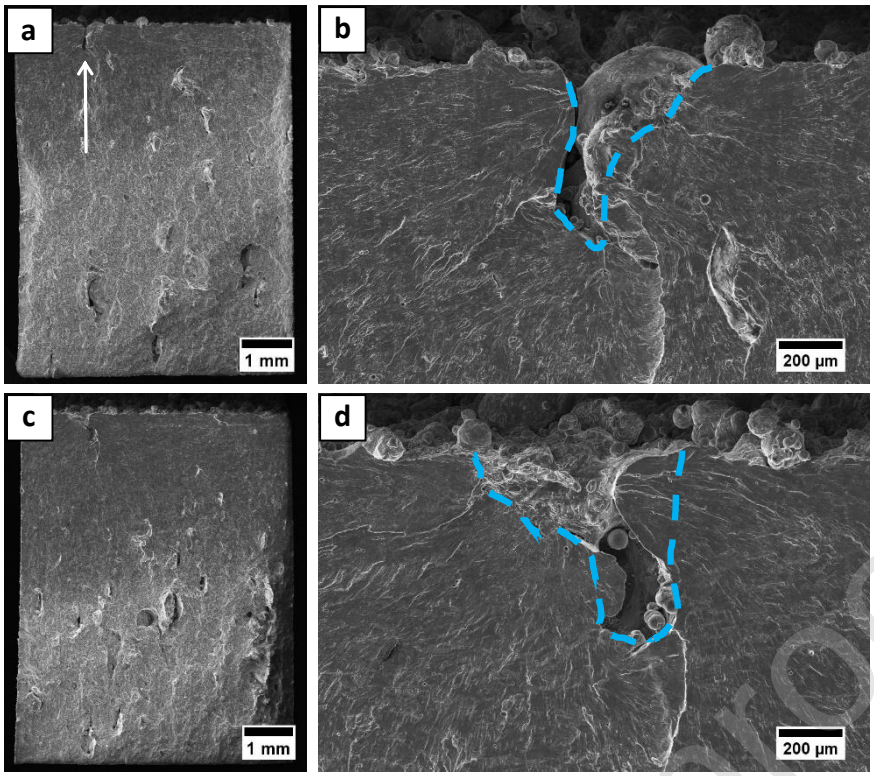


**Fig. 8.** SEM views of the fracture surfaces of two S01 specimens that failed due to VDs: samples tested at a stress of (a and b) 220 MPa and (c and d) 140 MPa. The blue dashed line represents the chosen area corresponding to the critical VDs.

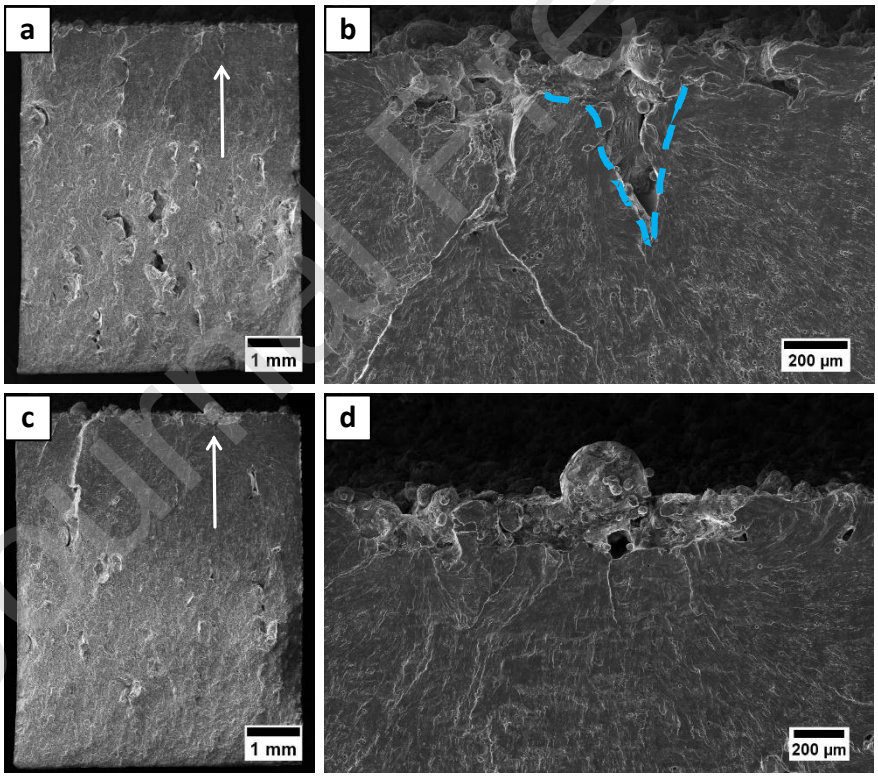


**Fig. 9.** SEM views of the fracture surfaces of the S05 specimens that failed due to (a and b) VDs at a stress of 180 MPa and (c and d) SFs at a stress of 140 MPa. The blue dashed line represents the chosen area corresponding to the critical VDs.

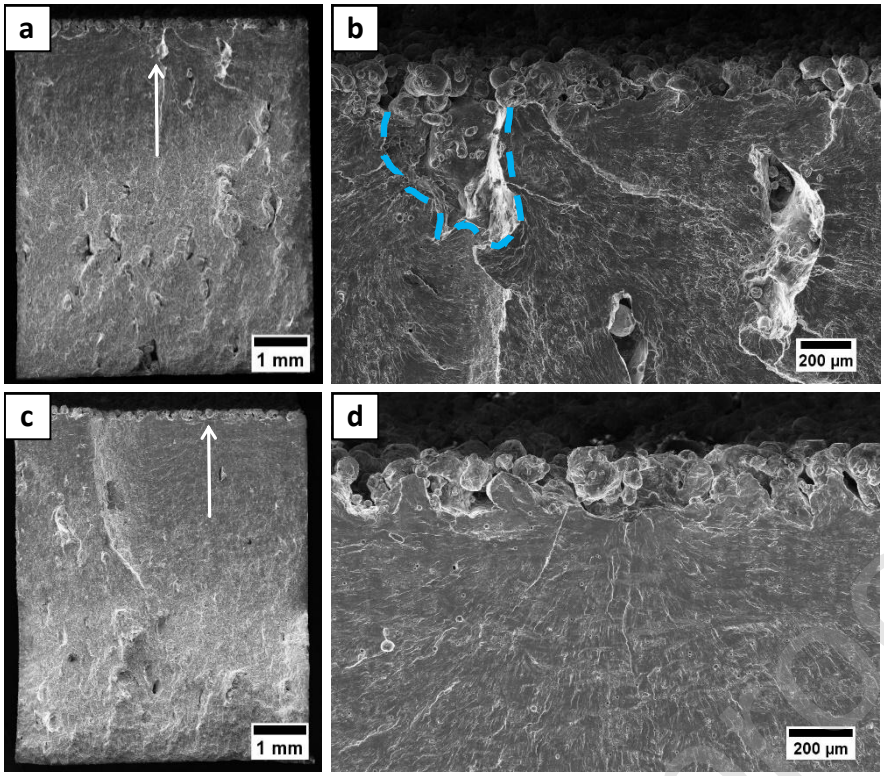


**Fig. 10.** SEM views of the fracture surfaces of the S07 specimens that failed due to (a and b) VDs at a stress of 220 MPa and (c and d) SFs at a stress of 140 MPa. The blue dashed line represents the chosen area corresponding to the critical VDs.

**Table 5** summarizes the sizes of the critical VDs measured on the fracture surfaces, as highlighted in **Figs. 8–10**. Note that in one S05 sample and one S07 sample, it was difficult to distinguish the critical defect type, so the numbers of failures from VDs or SFs were registered as ranges. It can be noted that, according to the measurements reported in Section 3.3, the number of failures caused by VDs decreases when the depth of the largest SFs increases, highlighting a form of competition between these two defect types on the fatigue-nucleation mechanism.

Considering that all of the batches were manufactured using the same parameters for the core, no variability of the VDs was expected among the batches. This feature was demonstrated by investigating the post-mortem fracture surfaces, which showed consistency in terms of the size of the maximum VD detected in every batch. Note that the competition between the two failure modes was responsible for the increase in the average size of the critical VDs from S01 to S07. In fact, in the presence of very deep SFs (i.e., in S05 and S07), failures due to VDs occurred only in the presence of very large flaws, which were more detrimental than the VDs. This kind of *high-pass filter* explains both the increase in the average size and the large standard deviation associated with the S01 samples.

| Surface code | Failures from VD | Maximum size (mm) | Average size (mm) | Standard deviation (mm) |
|---|---|---|---|---|
| **S01** | 9/9 | 0.524 | 0.353 | 0.115 |
| **S05** | 4-5/9 | 0.501 | 0.452 | 0.043 |
| **S07** | 2-3/9 | 0.579 | 0.532 | 0.067 |

**Table 5.** Summary of the size of critical VDs measured on the fracture surfaces (size in terms of $\sqrt{area}$).

Having verified the substantial correspondences of the VDs in the three batches, the surface texture achieved by modification of the process parameters remained the main distinctive factor affecting the failure of the samples. The sizes of the SFs at the origin of fatigue failure were measured as well. These measurements complemented the shapes of the SFs evaluated on the polished sections in the out-of-plane direction. Under the common assumption of semi-elliptical shape, the shape ratio $a/c$ was evaluated to be

in the range from 2 to 5, with $a$ and $c$ being the crack depth and semi-length, respectively. This method involves treating SFs as shallow surface cracks. According to fracture mechanics, the main parameter in evaluating the criticality of a crack subjected to a cyclic load is the stress intensity factor (SIF), which is defined as

$$K = Y\,\sigma\,\sqrt{\pi\,a}, \tag{3}$$

where $\sigma$ is the applied stress, $a$ is the crack size (in this case, the depth of the shallow crack), and $Y$ is the boundary correction factor (BCF), which depends on the shape, position, and cross-sectional size of the crack. According to the commonly used solutions by Newman and Raju [75], the BCF range for a shallow surface crack subjected to bending and having the experimentally determined shape ratio is $Y = (0.9, 1.1)$.

**4. Fracture mechanics analysis of surface and sub-surface irregularities**

To achieve better understanding of the effects of the various surface irregularities detected in the investigated samples, the stress intensity associated with the surface and sub-surface defects was calculated by finite element (FE) analyses. The steps performed in these simulations are listed below and summarized in **Fig. 11**:

1. Extract a relevant section of the surface (with a length of at least 1 mm);
2. Perform thresholding to distinguish the material from the background;
3. Mesh the image with a sufficiently large number of 2D FEs;
4. Import the mesh into an FE environment, define the load and boundary conditions, and prepare the FE analysis.

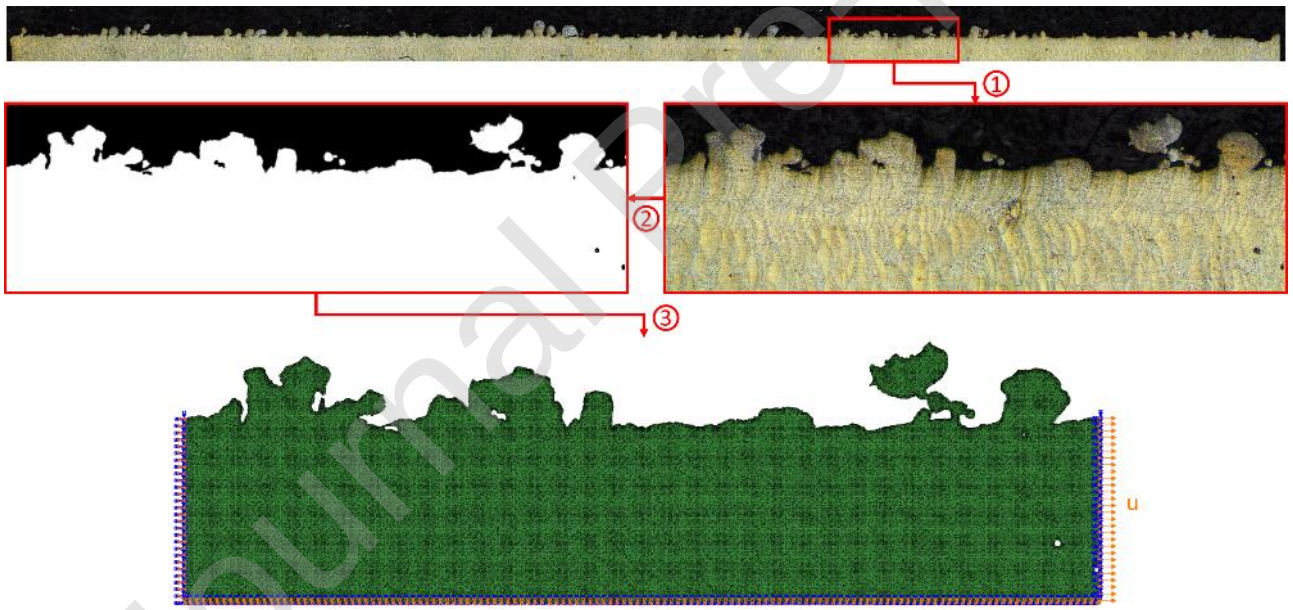


**Fig. 11.** Scheme of the steps adopted to perform the FE simulation, referring to the profile of the S01 samples.

In this investigation, after thresholding, the mesh was created using the BoneJ package of the ImageJ software, and the FE analysis was run in Abaqus 2017 using quadratic elements. The material was defined as linear-elastic, with a Young's modulus $E$ of 74 GPa and Poisson's ratio $\nu$ of $0.33$. Boundary conditions were applied to constrain the vertical displacement, rotation of the bottom surface, and horizontal displacement and rotation of the left surface. The strain was introduced by applying a unitary horizontal displacement to the right surface.

The results thus obtained are depicted in **Fig. 12** in terms of maximum principal stress. They clearly show that overhanging particles in the profile of S01 do not introduce any significant stress intensity (**Fig. 12a**), while the relatively flat surface in the rest of the sample ensures an almost homogeneous stress distribution. Considering the conditions of S05 (**Fig. 12b**), large stress intensities are caused by deep cavities and sub-surface pores. It is evident that the deepest features are the most critical flaws, whereas the shorter cavities are shielded by the largest ones. Regarding S07 (**Fig. 12c**), the outer layer is almost completely isolated from the bulk due to the presence of porosity and discontinuities located approximately 80 µm from the surface, i.e., the contour layer width. However, the maximum principal stress at the weakest point corresponds to values significantly lower than those estimated for the S05 samples. This difference can be supposed to be due to a sort of *shielding effect* promoted by the surface and sub-surface porosities. Considering the S01 samples, although no important stress intensity spots were highlighted, several weak spots are observable in the regions in which the surface porosity extends more deeply below the average surface line. This demonstrates that the depth measurements described in Section 3.3 can be used to evaluate the criticality of such features in terms of fracture mechanics.

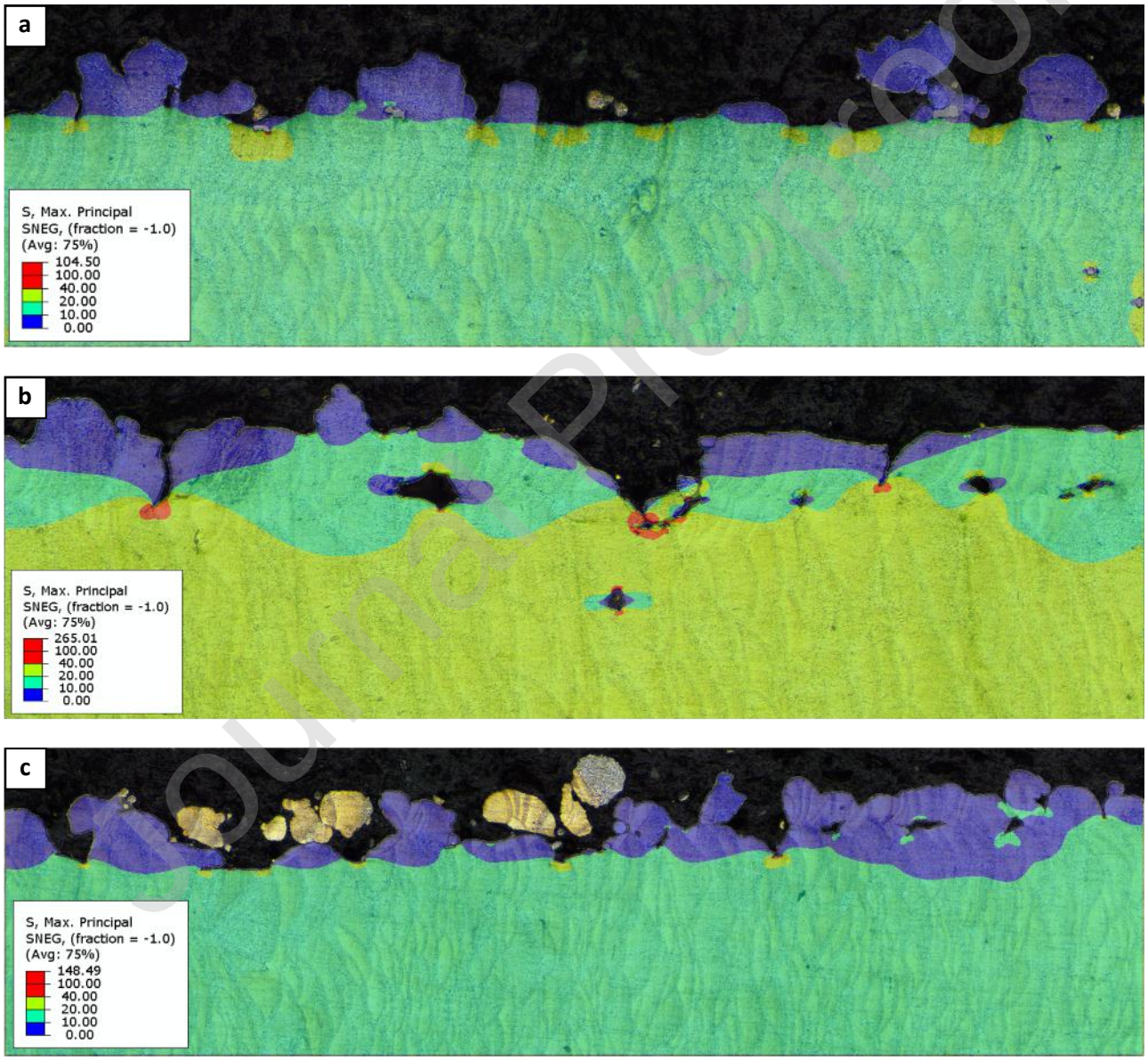


**Fig. 12.** Maximum principal stress obtained by FE simulations for the three sample batches: (a) S01, (b) S05, and (c) S07.

Regarding the other two conditions analyzed herein, their evaluation appears more complex, as the presence of frequent sub-surface pores and cavities introduces shielding effects, i.e., some of the surface is

substantially unloaded. Thus, simple depth measurements from the average line (see **Fig. 5**) for the S05 and S07 samples might not provide sufficiently precise evaluation for description of the effects of SFs from a fracture mechanics perspective. In fact, even though the maximum depth was measured to be quite similar under both conditions (see **Table 4**), the maximum principal stress resulting from the FE simulations yielded completely different results (see **Fig. 12**).

To overcome this limitation, a second set of FE analyses was performed, in which the deepest SFs were evaluated as one-dimensional cracks in a two-dimensional material under plane-strain conditions. A portion of 1.5 mm length was selected from the three polished sections depicted in **Fig. 5**. A refined quadratic mesh was adopted around the crack tips to ensure convergence of the SIF that was calculated using the integral contour algorithm. The problem was simplified from a geometrical perspective by considering a flat outer surface in correspondence to the previously described ideal average line. The effect of sub-surface pores was evaluated by placing similar features of simplified shapes in the same positions. The results thus obtained are depicted in **Fig. 13**.

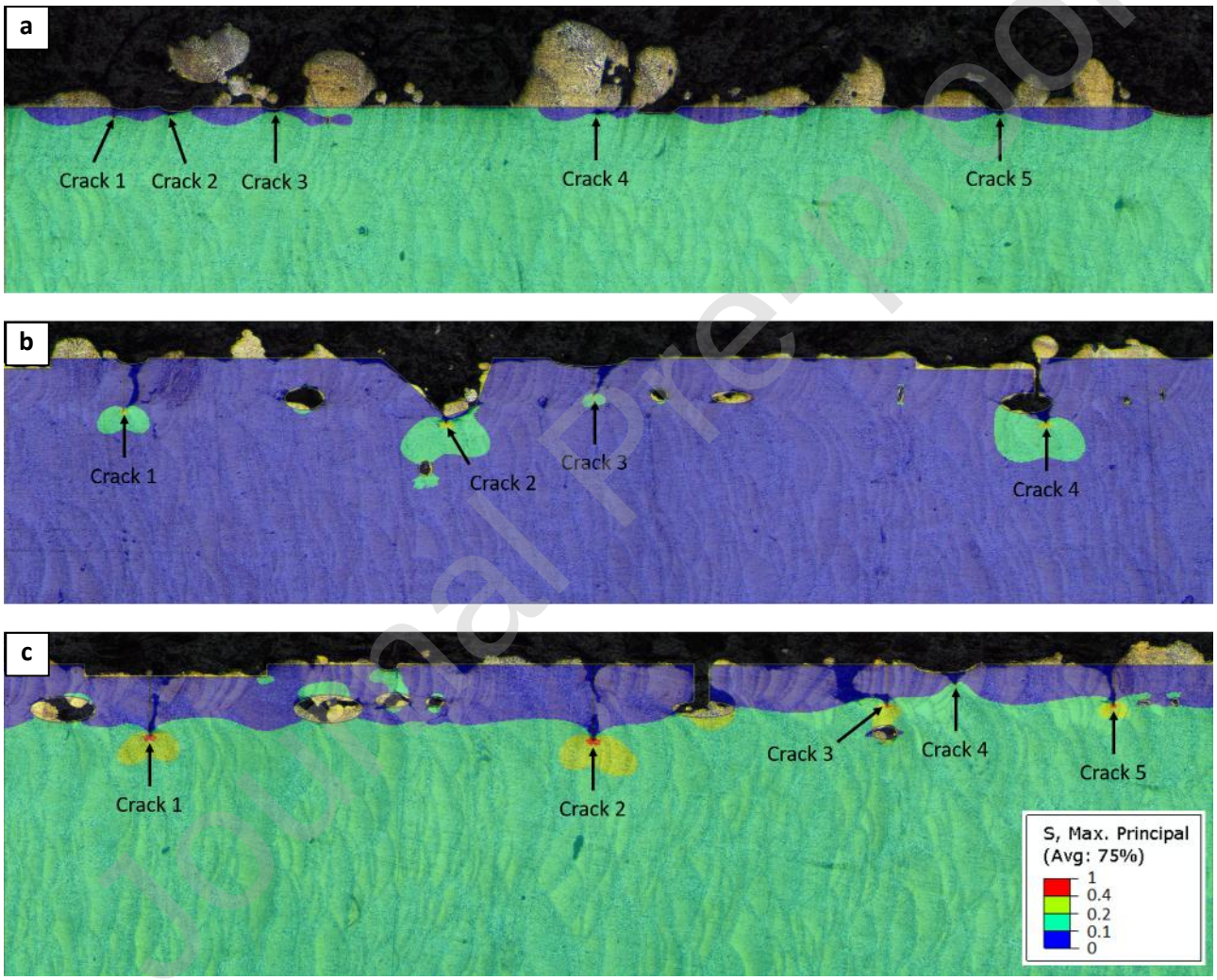


**Fig. 13.** Normalized maximum principal stress for the three batches of samples in the presence of surface cracks and sub-surface pores: (a) S01, (b) S05, and (c) S07.

The resulting stress field looks similar to that depicted in **Fig. 12** in terms of stress concentration. Based on the crack depth $a$ and SIF ($K$) evaluated by FE simulation of each crack, the BCF was determined by inverting Eq. (3) as follows:

$$Y = K/(\sigma\sqrt{\pi\, a}), \tag{4}$$

where, $\sigma$ is the nominal stress applied to the cross-section. Note that the *Y* values are not influenced by such stress, as the ratio $K/\sigma$ is constant for a given crack size. The results obtained are summarized in **Table 6**. The BCF values obtained from the shapes of the surface cracks in S01 fall within the (0.9, 1.1) range. In contrast, the simulations performed on the S05 and S07 samples yielded lower values, which were expected considering the previously described shielding effects caused by the sub-surface porosities near the modelled cracks.

| Condition | Crack # | 1 | 2 | 3 | 4 | 5 |
|---|---|---|---|---|---|---|
| **S01** | **a (µm)** | 22 | 18 | 12 | 15 | 17 |
| | **Y** | 1.06 | 0.93 | 1.04 | 1.15 | 1.09 |
| **S05** | **a (µm)** | 131 | 145 | 95 | 162 | |
| | **Y** | 0.88 | 0.95 | 0.71 | 0.87 | |
| **S07** | **a (µm)** | 148 | 156 | 84 | 40 | 84 |
| | **Y** | 0.80 | 0.82 | 0.75 | 0.43 | 0.80 |

**Table 6.** Results of FE simulations of crack effects.

The BCF for the deepest point of an isolated shallow surface crack is $Y \cong 1.12$ [75]. In **Fig. 14**, this reference value is compared with the results obtained from the FE simulations (see **Table 6**). **Fig. 14a** shows that the BCFs computed for the cracks in the S01 samples agree well with the hypothesis of shallow semi-elliptical surface cracks. In contrast, the BCFs computed for S05 and S07 are systematically smaller. This difference can be explained by the shielding effects introduced by the sub-surface features present in these samples, which agrees with the idea that the depth from an ideal outer surface is not sufficient to describe the criticality of a defect for the S05 and S07 samples. Therefore, based on the FE simulation results depicted in **Fig. 13**, the BCFs for S05 and S07 were re-computed considering an *empirical effective crack size*

$$a^* = a - w/2, \tag{6}$$

where $w \cong 80$ µm is the width of the contour layer. A method of linking the size of surface cracks due to coarse surface finish to the dimensions of the contour layer was also reported in [65]. **Fig. 14b** shows that all of the re-calculated FE results approach the reference value and have the same variability as the S01 data. Moreover, they are consistent with the BCF range estimated based on the shape of the critical surface cracks, i.e., [0.9, 1.1], that was mentioned in Section 3.5.

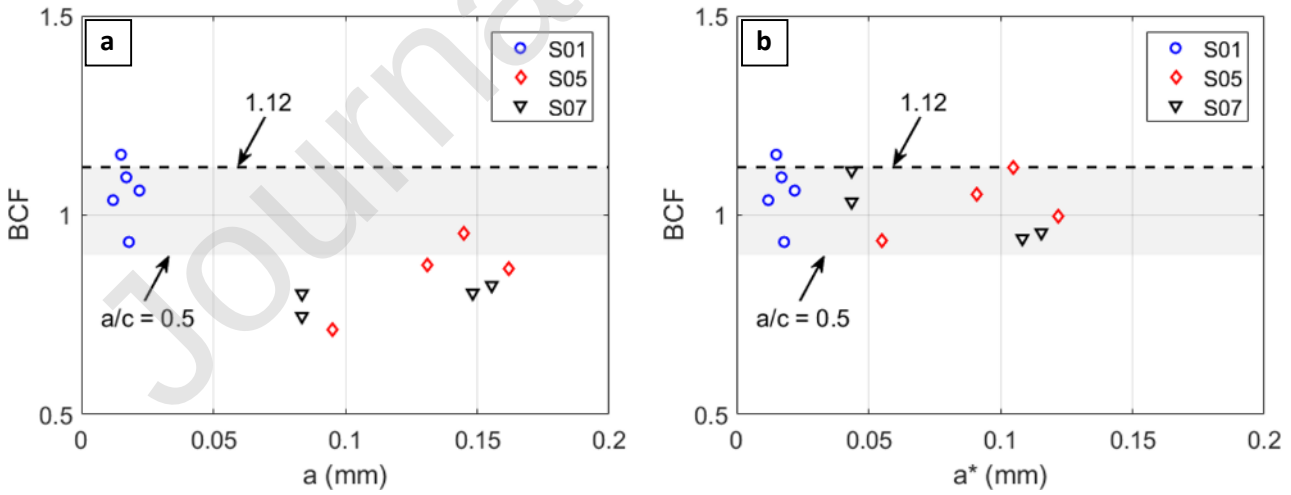


**Fig. 14.** BCF for SIF calculation evaluated from FE simulations: (a) crack depth from the outer surface and (b) effective crack depth considering the shielding effects.

## 5. Discussion

Based on the topological measurements of the SFs, one could expect that a surface having large roughness peaks, such as S01, would be more detrimental than one featuring lower roughness, such as S07. Conversely,

fractography analyses of the fatigue-tested specimens showed that all of the failures detected in S01 were caused by VDs, while only a small percentage of internal defects (specifically LoF) occurred at the fracture origin of the S07 samples.

The reason for this finding is that the large peaks in the S01 surface profiles were caused by partially melted particles and large spatter stuck on the surface, which neither carry any load nor introduce any stress concentration in the material, while the rest of the surface is almost flat and homogeneous. In contrast, the top layer of S07 appears smooth externally, but it is almost detached from the internal material volume because of the presence of several sub-surface cavities (see **Fig. 5c**). As clearly demonstrated in **Figs. 9d** and **10**, these cavities are very detrimental to the fatigue properties. Moreover, standard contact and non-contact techniques are blind to the detection of these defect types, which is why the arithmetical mean height parameters must be considered improper variables or used cautiously to explain the complexity of AM surfaces.

Different metrological methods demonstrated that, on L-PBF, part surfaces with low contour line energies could generate low arithmetical mean height ($R_a$ and $S_a$) parameters, using a stylus-based, non-contact profilometer. Nonetheless, opposite conclusions can be drawn using the other two parameters investigated by both measurement techniques (**Figs. 3a** and **3b**). The combination of *RPc* and *RSm* could quantitatively explain the qualitative representation obtained using the SEM (**Fig. 2**) and the areal surfaces constructed using confocal microscopy (**Fig. 4**) [24]. It is also notable that working with a stylus could raise surface-related concerns due to the low hardness of Al alloys, which is why special attention is needed in the selection of stylus radii and contact forces [76]. *Ssk* turned out to be able to distinguish between the bulk surfaces (S01–S04) with positive skewness and porous surfaces (S05–S07) with negative skewness. *Sv* could accurately describe the extent of the deepest surface cavities in almost all cases. However, confocal microscopy measurements are not suitable for identifying the largest cavities integrated with undercuts. Therefore, to get as close as possible to the real value, a large test field area is highly recommended.

However, none of the aforementioned measurement techniques could provide insight into the AMZ, such as the effects of undercuts [25], to prove the appropriateness of the measurements. Therefore, it is recommended to perform a more accurate study of the SFs accompanied by cross-sectional analyses.

*5.1 Surface quality improvement*

Given the important differences among the investigated sample batches in terms of the SF size and defect shapes, knowledge about the depth of the AMZ is fundamental in applications requiring controlled surface-related defects. Indeed, an inappropriate surface removal depth can have detrimental effects on the fatigue lives, which are very similar to those of the as-built specimens [77].

The large AMZ in the S05 and S07 specimens can be ascribed to the insufficient contour melt pool width, which is unable to repair the defects generated by the last volume scan and introduces even more segmentation due to balling effects [78]. Therefore, before the surface finishing of AM parts, it is important to determine the actual extent of the AMZ by performing cross-sectional image analysis or X-ray µCT [66].

Based on the results summarized in **Table 4**, removing a 60-µm-thick layer of material from the surfaces of the S01 samples would ensure the removal of almost all the surface flaws. However, no fatigue performance improvement is expected, as the failure cause for this condition was always a VD. Regarding the S07 samples, a removal of at least 200 µm of the surface is expected to be necessary to avoid failures from the surface.

*5.2 Crack size evaluation for SFs*

The FE analyses presented in Section 4 highlighted the very detrimental effect of shallow features extending deep inside the bulk material, which are the preferential spots for early nucleation of fatigue

cracks. After crack nucleation from such features due to the high local stress intensity, the fatigue resistance of the material is negatively affected, where only at least one of these cracks has enough energy to begin propagating. From a fracture mechanics approach, both VDs and SFs can be regarded as short cracks, and fatigue failure is expected from the cracks subjected to the largest SIF. By adopting the widely accepted model of Murakami, based on the $\sqrt{\text{area}}$ parameter [51] (see Eq. (3)), both VDs and SFs can be treated simply as surface cracks subjected to the nominal stress in the sample, i.e., the largest SIF corresponds to the largest size in terms of $\sqrt{\text{area}}$.

Therefore, to perform one-to-one competing risk analysis of the criticality of VDs and SFs, it is necessary to compare the sizes of such defects in terms of $\sqrt{\text{area}}$. However, the SF measurements performed on the polished sections only describe the depth of the surface shallow cracks. Therefore, the shapes and sizes of such cracks must be defined in the direction perpendicular to the polished sections. In the following, the empirical relationship

$$\sqrt{\text{area}} = \sqrt{10}\, a^* \tag{5}$$

proposed by Murakami [51] is adopted, which is valid for very slender surface cracks and for surface roughness evaluation [79,80], where the effective crack depth $a^*$ is adopted to account for the shielding effects described in Section 4. This formulation is consistent with the upper limit of the BCF range in **Fig. 14**, i.e., $Y = 1.12$.

*5.3 Probabilistic competing-risk assessment*

A simple and commonly used method of estimating the fatigue resistances of notched parts in the presence of manufacturing defects involves considering the largest defect falling inside the 90% volume, i.e., the volume subjected to at least 90% of the maximum applied stress [81–84]. For the bending samples investigated in this study, this volume is highlighted in red in **Fig. 15**. All of the critical VDs affecting the fracture nucleation are inside the red regions of the tested samples, confirming the applicability of this approach. By applying the same logic to the critical SFs, the critical surface length $l_{90}$ subjected to at least 90% of the maximum applied stress was evaluated by FE analysis (see **Fig. 15**), and $l_{90} = 3.4$ mm was obtained.

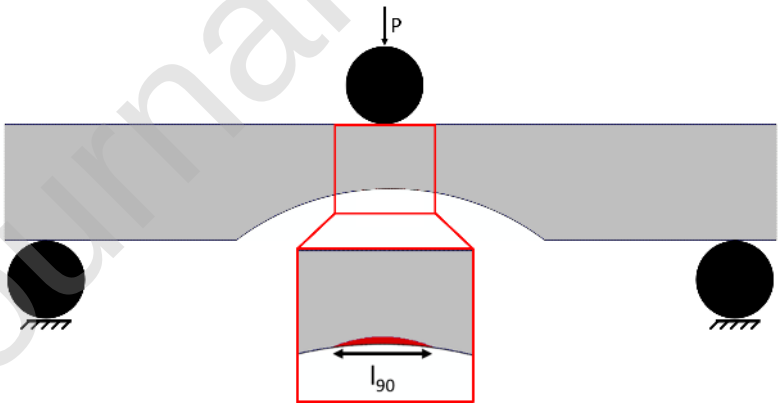


**Fig. 15.** Length of the surface region subjected to at least 90% of the maximum applied stress, as defined by FE simulation.

To evaluate which of the two defect types is more critical for a certain batch of samples, the largest VD falling inside $V_{90}$ is compared to the largest SF within $l_{90}$. The former dimension was obtained by measuring the size of the critical VDs on the fracture surfaces (see **Table 5**), while the latter could be estimated by applying statistics of extremes. In fact, knowing the size distribution of the largest feature sampled in the reference surface length $l_0$, the distribution of the maximum size for a length $l_{90}$ could be obtained as follows:

$$F(l_{90}) = F(l_0)^{l_{90}/l_0}, \tag{7}$$

where $l_{90}/l_0 = 3.4$ mm is the *return period* of the maximum defect and $F$ is the cdf, which describes the data collected.

The 20 measurements per surface condition collected as described in Section 3.3 were recalculated in terms of $\sqrt{\text{area}}$ using Eq. (5) and fitted with the LEVD as depicted in **Fig. 16a**. The data were then shifted to obtain the maximum size related to a surface length $l_{90}$ according to Eq. (7). The parameters of the critical defect distributions obtained for the samples investigated are reported in **Table 7**. **Fig. 16b** shows the distributions of the maximum critical SF expected in the samples compared to the critical VD size distribution. The latter distribution was described as an LEVD fitted on the experimental measurements performed for condition S01 (see **Table 5**), as this was the only condition in which no failures occurred due to SFs.

| **Defect type** | **Volumetric** | **Surface** | | |
|---|---|---|---|---|
| **Condition** | **All** | **S01** | **S05** | **S07** |
| **λ (mm)** | 0.301 | 0.094 | 0.259 | 0.382 |
| **δ (mm)** | 0.090 | 0.027 | 0.094 | 0.064 |

**Table 7.** LEVD parameters for critical VD and SF sizes for the bending samples tested.

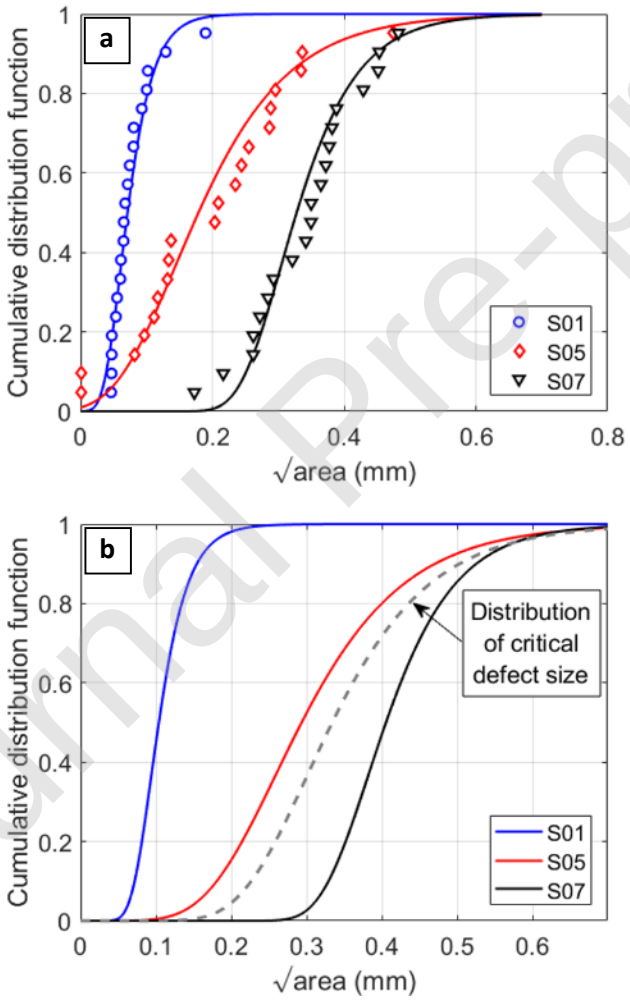


**Fig. 16.** Probabilistic analysis results: (a) LEVD of maximum SFs measured on polished sections; (b) competing-risk assessment of critical VDs and SFs in the samples.

The probability of experiencing a fatigue failure caused by an SF rather than a VD is then the probability that the largest SF contained in the critical region of the sample ($\sqrt{\text{area}}_{\text{SF}}$) is larger than the largest VD size ($\sqrt{\text{area}}_{\text{VD}}$), i.e.,

$$P_{f,\text{SF}} = \Pr\{\sqrt{\text{area}}_{\text{SF}} > \sqrt{\text{area}}_{\text{VD}}\}. \tag{8}$$

This probability can be determined by solving the integral

$$P_{f,\mathrm{SF}} = \int_0^{+\infty} f_{\mathrm{VD}}(x)\,[1 - F_{\mathrm{SF}}(x)], \tag{9}$$

where $F_{\mathrm{SF}}$ is the cdf of the maximum SF size and $f_{\mathrm{VD}}$ is the probability density function of the experimental VD size distribution (all LEVD parameters are reported in **Table 7**). Eq. (9) was numerically solved using the integral transform method [85], which provided the probability values summarized in **Table 8**. Even considering the variability sources involved and the inaccuracies of the manual measurements, the estimates provide a satisfactory description of the *competing risk* between VDs and poor surface quality.

| Sample code | Experimental | Estimated |
|---|---|---|
| **S01** | 0% | 0% |
| **S05** | 44-55% | 39% |
| **S07** | 67-78% | 71% |

**Table 8.** Comparison of experimental and estimated probabilities of failures due to SFs.

## 6. Conclusions

The effects of the surface conditions on the fatigue properties of L-PBF AlSi7Mg were investigated considering samples fabricated with different process parameters for the contour layers, resulting in different surface characteristics. The quality of the surfaces was then investigated using contact and non-contact metrological methods, followed by analysis of the polished cross-sections. The fracture surfaces were carefully investigated after performing bending fatigue tests on three sets of samples. The mechanical effects of the investigated SFs were evaluated by conducting FE simulations aimed at determining the stress concentration and SIF. Finally, a competing-risk fracture mechanics assessment method was developed and validated. The proposed approach enabled us to compare the criticality of VDs and surface flaws.

The following conclusions were drawn.

- Contact and non-contact roughness measurements cannot describe all of the typical fatigue-critical features introduced by AM processes. More comprehensive information can be obtained by analyzing polished cross-sections.
- The maximum valley depth *Sv* can describe the deepest valley based on the chosen test field area.
- Evaluating the size of the most critical defect is essential for correct fatigue assessment. The flaw size can be measured using the $\sqrt{\mathrm{area}}$ parameter considering VDs, or the depth of the SFs.
- The presence of multiple surface and sub-surface flaws can create beneficial shielding effects; therefore, simple measurement of the crack depth from the outer surface might not guarantee correct quality assessment.
- A simple empirical relationship was proposed to evaluate the above shielding effects by considering the *effective crack depth*.
- More precise SIF assessment for the surface conditions investigated was achieved using a simple fracture mechanics model based on defect depth measurements performed on polished cross-sections. It was thus possible to describe the competition between the VDs and SFs correctly for the three batches of samples investigated.

## Acknowledgements

The support by the Italian Ministry for Education, University and Research (MIUR) through the project “Department of Excellence LIS4.0” (Integrated Laboratory for Lightweight and Smart Structures) is acknowledged.

**7. References**


[1] T. DebRoy, H.L. Wei, J.S. Zuback, T. Mukherjee, J.W. Elmer, J.O. Milewski, A.M. Beese, A. Wilson-Heid, A. De, W. Zhang, Additive manufacturing of metallic components – Process, structure and properties, Prog. Mater. Sci. 92 (2018) 112–224. doi:10.1016/j.pmatsci.2017.10.001.

[2] D. Herzog, V. Seyda, E. Wycisk, C. Emmelmann, Additive manufacturing of metals, Acta Mater. (2016). doi:10.1016/j.actamat.2016.07.019.

[3] A. Bandyopadhyay, B. Heer, Additive manufacturing of multi-material structures, Mater. Sci. Eng. R Reports. (2018). doi:10.1016/j.mser.2018.04.001.

[4] D.D. Gu, W. Meiners, K. Wissenbach, R. Poprawe, Laser additive manufacturing of metallic components: materials, processes and mechanisms, Int. Mater. Rev. 57 (2012) 133–164. doi:10.1179/1743280411Y.0000000014.

[5] K. Alrbaey, D. Wimpenny, R. Tosi, W. Manning, A. Moroz, On optimization of surface roughness of selective laser melted stainless steel parts: A statistical study, J. Mater. Eng. Perform. 23 (2014) 2139–2148. doi:10.1007/s11665-014-0993-9.

[6] Y. Tian, D. Tomus, P. Rometsch, X. Wu, Influences of processing parameters on surface roughness of Hastelloy X produced by selective laser melting, Addit. Manuf. (2017). doi:10.1016/j.addma.2016.10.010.

[7] W. Yu, S.L. Sing, C.K. Chua, X. Tian, Influence of re-melting on surface roughness and porosity of AlSi10Mg parts fabricated by selective laser melting, J. Alloys Compd. 792 (2019) 574–581. doi:10.1016/J.JALLCOM.2019.04.017.

[8] Y. Kaynak, O. Kitay, The effect of post-processing operations on surface characteristics of 316L stainless steel produced by selective laser melting, Addit. Manuf. (2019). doi:10.1016/j.addma.2018.12.021.

[9] Y. Pupo, K.P. Monroy, J. Ciurana, Influence of process parameters on surface quality of CoCrMo produced by selective laser melting, Int. J. Adv. Manuf. Technol. (2015). doi:10.1007/s00170-015-7040-3.

[10] M. Hamidi Nasab, A. Falzetti, A. Redaelli, N. Lecis, A. Giussani, L. Sala, M. Vedani, Finishing of internal and external surfaces produced by Powder Bed Fusion, in: SIG Addit. Manuf., 2017.

[11] P.D. Nezhadfar, R. Shrestha, N. Phan, N. Shamsaei, Fatigue behavior of additively manufactured 17-4 PH stainless steel: Synergistic effects of surface roughness and heat treatment, Int. J. Fatigue. 124 (2019) 188–204. doi:10.1016/j.ijfatigue.2019.02.039.

[12] C. Zhang, H. Zhu, H. Liao, Y. Cheng, Z. Hu, X. Zeng, Effect of heat treatments on fatigue property of selective laser melting AlSi10Mg, Int. J. Fatigue. 116 (2018) 513–522. doi:10.1016/j.ijfatigue.2018.07.016.

[13] Q. Han, Y. Jiao, Effect of heat treatment and laser surface remelting on AlSi10Mg alloy fabricated by selective laser melting, Int. J. Adv. Manuf. Technol. (2019). doi:10.1007/s00170-018-03272-y.

[14] A.H. Maamoun, Y.F. Xue, M.A. Elbestawi, S.C. Veldhuis, Effect of selective laser melting process parameters on the quality of al alloy parts: Powder characterization, density, surface roughness, and dimensional accuracy, Materials (Basel). (2018). doi:10.3390/ma11122343.

[15] T. Yang, T. Liu, W. Liao, E. MacDonald, H. Wei, X. Chen, L. Jiang, The influence of process parameters on vertical surface roughness of the AlSi10Mg parts fabricated by selective laser melting, J. Mater. Process. Technol. (2019). doi:10.1016/j.jmatprotec.2018.10.015.

[16] A. Maamoun, M. Elbestawi, S. Veldhuis, Influence of Shot Peening on AlSi10Mg Parts Fabricated by

Additive Manufacturing, J. Manuf. Mater. Process. (2018). doi:10.3390/jmmp2030040.

[17] M. Hamidi Nasab, D. Gastaldi, N.F. Lecis, M. Vedani, On morphological surface features of the parts printed by selective laser melting (SLM), Addit. Manuf. 24 (2018) 373–377. doi:10.1016/j.addma.2018.10.011.

[18] I. Yadroitsev, I. Smurov, Surface morphology in selective laser melting of metal powders, in: Phys. Procedia, 2011. doi:10.1016/j.phpro.2011.03.034.

[19] A. Townsend, N. Senin, L. Blunt, R.K. Leach, J.S. Taylor, Surface texture metrology for metal additive manufacturing: a review, Precis. Eng. 46 (2016) 34–47. doi:10.1016/j.precisioneng.2016.06.001.

[20] J.S. Taylor, Physical processes linking input parameters and surface morphology in additive manufacturing, in: Proc. - ASPE 2015 Spring Top. Meet. Achiev. Precis. Toler. Addit. Manuf., 2015: pp. 70–71.

[21] L. zhi Wang, S. Wang, J. jiao Wu, Experimental investigation on densification behavior and surface roughness of AlSi10Mg powders produced by selective laser melting, Opt. Laser Technol. 96 (2017) 88–96. doi:10.1016/j.optlastec.2017.05.006.

[22] K. Mumtaz, N. Hopkinson, Top surface and side roughness of Inconel 625 parts processed using selective laser melting, Rapid Prototyp. J. 15 (2009) 96–103. doi:10.1108/13552540910943397.

[23] G. Strano, L. Hao, R.M. Everson, K.E. Evans, Surface roughness analysis, modelling and prediction in selective laser melting, J. Mater. Process. Technol. 213 (2013) 589–597. doi:10.1016/j.jmatprotec.2012.11.011.

[24] J.C. Fox, S.P. Moylan, B.M. Lane, Effect of Process Parameters on the Surface Roughness of Overhanging Structures in Laser Powder Bed Fusion Additive Manufacturing, in: Procedia CIRP, 2016: pp. 131–134. doi:10.1016/j.procir.2016.02.347.

[25] G.T. Smith, Machined surface integrity, in: G.T. Smith (Ed.), Ind. Metrol. Surfaces Roundness, Springer London, London, 2002: pp. 185–247. doi:10.1007/978-1-4471-3814-3_5.

[26] S. Bagehorn, J. Wehr, H.J. Maier, Application of mechanical surface finishing processes for roughness reduction and fatigue improvement of additively manufactured Ti-6Al-4V parts, Int. J. Fatigue. 102 (2017) 135–142. doi:10.1016/j.ijfatigue.2017.05.008.

[27] J. Pegues, M. Roach, R.S. Williamson, N. Shamsaei, Surface Roughness Effects on the Fatigue Strength of Additively Manufactured Ti-6Al-4V, Int. J. Fatigue. 116 (2018) 543–552. doi:https://doi.org/10.1016/j.ijfatigue.2018.07.013.

[28] R.K. Leach, N. Senin, A metrology horror story: the additive surface, in: ASPEN/ASPE Spring Top. Meet. 2017-Manufacture Metrol. Struct. Free. Surfaces Funct. Appl., Honk Kong, 2017. https://www.researchgate.net/publication/314184961_A_metrology_horror_story_the_additive_surface.

[29] D.B. Witkin, D.N. Patel, H. Helvajian, L. Steffeney, A. Diaz, Surface Treatment of Powder-Bed Fusion Additive Manufactured Metals for Improved Fatigue Life, J. Mater. Eng. Perform. 28 (2019) 681–692. doi:10.1007/s11665-018-3732-9.

[30] K. Mumtaz, N. Hopkinson, Top surface and side roughness of Inconel 625 parts processed using selective laser melting, Rapid Prototyp. J. 15 (2009) 96–103. doi:10.1108/13552540910943397.

[31] A. Triantaphyllou, C.L. Giusca, G.D. Macaulay, F. Roerig, M. Hoebel, R.K. Leach, B. Tomita, K.A. Milne, Surface texture measurement for additive manufacturing, Surf. Topogr. Metrol. Prop. 3 (2015). doi:10.1088/2051-672X/3/2/024002.

[32] E. Yasa, J. Kruth, Application of Laser Re-Melting on Selective Laser Melting Parts, Adv. Prod. Eng.

Manag. (2011).

[33] F. Calignano, D. Manfredi, E.P. Ambrosio, L. Iuliano, P. Fino, Influence of process parameters on surface roughness of aluminum parts produced by DMLS, Int. J. Adv. Manuf. Technol. 67 (2013). doi:10.1007/s00170-012-4688-9.

[34] R.I. Campbell, M. Martorelli, H.S. Lee, Surface roughness visualisation for rapid prototyping models, CAD Comput. Aided Des. (2002). doi:10.1016/S0010-4485(01)00201-9.

[35] E. Abele, M. Kniepkamp, Analysis and optimisation of vertical surface roughness in micro selective laser melting, Surf. Topogr. Metrol. Prop. 3 (2015) 034007. doi:10.1088/2051-672X/3/3/034007.

[36] A. Thompson, N. Senin, I. Maskery, L. Körner, S. Lawes, R. Leach, Internal surface measurement of metal powder bed fusion parts, Addit. Manuf. 20 (2018) 126–133. doi:10.1016/j.addma.2018.01.003.

[37] T. Grimm, G. Wiora, G. Witt, Characterization of typical surface effects in additive manufacturing with confocal microscopy, Surf. Topogr. Metrol. Prop. 3 (2015). doi:10.1088/2051-672X/3/1/014001.

[38] H. Galarraga, D.A. Lados, R.R. Dehoff, M.M. Kirka, P. Nandwana, Effects of the microstructure and porosity on properties of Ti-6Al-4V ELI alloy fabricated by electron beam melting (EBM), Addit. Manuf. 10 (2016) 47–57. doi:https://doi.org/10.1016/j.addma.2016.02.003.

[39] M.-H. Hong, B. Min, T.-Y. Kwon, The Influence of Process Parameters on the Surface Roughness of a 3D-Printed Co–Cr Dental Alloy Produced via Selective Laser Melting, Appl. Sci. (2016). doi:10.3390/app6120401.

[40] A. Temmler, E. Willenborg, K. Wissenbach, Laser polishing, in: 2012: pp. 82430W-8243–13. https://doi.org/10.1117/12.906001.

[41] G. Kerckhofs, G. Pyka, M. Moesen, S. Van Bael, J. Schrooten, M. Wevers, High-resolution microfocus X-ray computed tomography for 3d surface roughness measurements of additive manufactured porous materials, Adv. Eng. Mater. 15 (2013) 153–158. doi:10.1002/adem.201200156.

[42] G. Pyka, G. Kerckhofs, I. Papantoniou, M. Speirs, J. Schrooten, M. Wevers, Surface Roughness and Morphology Customization of Additive Manufactured Open Porous Ti6Al4V Structures, Mater. . 6 (2013). doi:10.3390/ma6104737.

[43] A. du Plessis, I. Yadroitsev, I. Yadroitsava, S.G. Le Roux, X-Ray Microcomputed Tomography in Additive Manufacturing: A Review of the Current Technology and Applications, 3D Print. Addit. Manuf. (2018) 3dp.2018.0060. doi:10.1089/3dp.2018.0060.

[44] A. du Plessis, S.G. le Roux, Standardized X-ray tomography testing of additively manufactured parts: A round robin test, Addit. Manuf. 24 (2018) 125–136. doi:https://doi.org/10.1016/j.addma.2018.09.014.

[45] J.N. Domfang Ngnekou, Y. Nadot, G. Henaff, J. Nicolai, W.H. Kan, J.M. Cairney, L. Ridosz, Fatigue properties of AlSi10Mg produced by Additive Layer Manufacturing, Int. J. Fatigue. 119 (2019) 160–172. doi:10.1016/j.ijfatigue.2018.09.029.

[46] C.A. Kantzos, R.W. Cunningham, V. Tari, A.D. Rollett, Characterization of metal additive manufacturing surfaces using synchrotron X-ray CT and micromechanical modeling, Comput. Mech. 61 (2017) 575–580. doi:10.1007/s00466-017-1531-z.

[47] B. Torries, A. Imandoust, S. Beretta, S. Shao, N. Shamsaei, Overview on Microstructure- and Defect-Sensitive Fatigue Modeling of Additively Manufactured Materials, Jom. 70 (2018) 1853–1862. doi:10.1007/s11837-018-2987-9.

[48] S. Beretta, S. Romano, A comparison of fatigue strength sensitivity to defects for materials manufactured by AM or traditional processes, Int. J. Fatigue. (2017).

doi:10.1016/j.ijfatigue.2016.06.020.

[49] A. Yadollahi, N. Shamsaei, Additive Manufacturing of Fatigue Resistant Materials: Challenges and Opportunities, Int. J. Fatigue. 98 (2017) 14–31. doi:10.1016/j.ijfatigue.2017.01.001.

[50] S. Romano, A. Brückner-Foit, A. Brandão, J. Gumpinger, T. Ghidini, S. Beretta, Fatigue properties of AlSi10Mg obtained by additive manufacturing: Defect-based modelling and prediction of fatigue strength, Eng. Fract. Mech. (2018). doi:10.1016/j.engfracmech.2017.11.002.

[51] Y. Murakami, Metal fatigue: effects of small defects and nonmetallic inclusions, Elsevier, 2002.

[52] Y. Yamashita, T. Murakami, R. Mihara, M. Okada, Y. Murakami, Defect analysis and fatigue design basis for Ni-based superalloy 718 manufactured by selective laser melting, Int. J. Fatigue. 117 (2018) 485–495. doi:10.1016/j.ijfatigue.2018.08.002.

[53] T. Persenot, A. Burr, G. Martin, J.-Y. Buffière, R. Dendievel, E. Maire, Effect of build orientation on the fatigue properties of as-built Electron Beam Melted Ti-6Al-4V alloy, Int. J. Fatigue. 118 (2018) 65–76. doi:10.1016/j.ijfatigue.2018.08.006.

[54] S. Romano, S. Miccoli, S. Beretta, A new FE post-processor for probabilistic fatigue assessment in the presence of defects and its application to AM parts, Accept. Int. J. Fatigue. (2019).

[55] S. Romano, L. Patriarca, S. Foletti, S. Beretta, LCF behaviour and a comprehensive life prediction model for AlSi10Mg obtained by SLM, Int. J. Fatigue. 117 (2018) 47–62. doi:10.1016/j.ijfatigue.2018.07.030.

[56] A. Yadollahi, M.J. Mahtabi, A. Khalili, H.R. Doude, J.C.J. Newman, Fatigue life prediction of additively manufactured material: Effects of surface roughness, defect size, and shape, Fatigue Fract. Eng. Mater. Struct. (2018) 1–13. doi:10.1111/ffe.12799.

[57] J.W. Pegues, N. Shamsaei, M.D. Roach, R.S. Williamson, Fatigue life estimation of additive manufactured parts in the as-built surface condition, Mater. Des. Process. Commun. (2019) e36. doi:10.1002/mdp2.36.

[58] E.W. Hovig, A.S. Azar, M.F. Sunding, K. Sørby, M. M'hamdi, E. Andreassen, High cycle fatigue life estimation of AlSi10Mg processed by laser powder bed fusion, MATEC Web Conf. 03015 (2018). doi:10.1051/matecconf/201818803015.

[59] B. Vayssette, N. Saintier, C. Brugger, M. Elmay, E. Pessard, Surface roughness of Ti-6Al-4V parts obtained by SLM and EBM: Effect on the High Cycle Fatigue life, Procedia Eng. 213 (2018) 89–97. doi:10.1016/j.proeng.2018.02.010.

[60] Y. Yamashita, T. Murakami, R. Mihara, M. Okada, Y. Murakami, Defect Analysis and Fatigue Design Basis for Ni-based Superalloy 718 manufactured by Additive Manufacturing, Int. J. Fatigue. (2018). doi:10.1016/j.prostr.2017.11.054.

[61] S. Romano, A. Abel, J. Gumpinger, A.D. Brandão, S. Beretta, Quality control of AlSi10Mg produced by SLM: metallography versus CT scans for critical defect size assessment, Addit. Manuf. (2019). doi:10.1016/j.addma.2019.05.017.

[62] J. Gumpinger, A.D. Brandao, E. Beevers, T. Rohr, T. Ghidini, S. Beretta, S. Romano, Expression of Additive Manufacturing Surface Irregularities Through a flaw-Based Assessment, Accept. ASTM Sel. Tech. Pap. (2019).

[63] H. Masuo, Y. Tanaka, S. Morokoshi, H. Yagura, T. Uchida, Y. Yamamoto, Y. Murakami, Influence of defects, surface roughness and HIP on the fatigue strength of Ti-6Al-4V manufactured by additive manufacturing, Int. J. Fatigue. 117 (2018) 163–179. doi:10.1016/j.ijfatigue.2018.07.020.

[64] D. Greitemeier, C. Dalle Donne, F. Syassen, J. Eufinger, T. Melz, Effect of surface roughness on fatigue performance of additive manufactured Ti-6Al-4V, Mater. Sci. Technol. 32 (2015) 629–634.

doi:10.1179/1743284715Y.0000000053.

[65] S. Romano, P.D. Nezhadfar, S. Beretta, M. Seifi, N. Shamsaei, High cycle fatigue behavior and life prediction for additively manufactured 17-4 PH stainless steel: Effect of sub-surface porosity and surface roughness, Submitt. to Addit. Manuf. (2019).

[66] S. Romano, A.D. Brandão, J. Gumpinger, M. Gschweitl, S. Beretta, Qualification of AM parts: Extreme value statistics applied to tomographic measurements, Mater. Des. 131 (2017) 32–48. doi:10.1016/j.matdes.2017.05.091.

[67] ISO 4288:1996 Geometrical Product Specifications (GPS), Surface texture: Profile method-Rules and procedures for the assessment of surface texture (ISO 4288: 1996), in: Ger. Version EN ISO, 1997. doi:10.1186/s40557-016-0111-6.

[68] International Organization for Standardization, ISO 25178-2: Geometrical product specifications (GPS) - Surface texture: Areal Part 2: Terms, definitions and surface texture parameters, 2007.

[69] L. Boniotti, S. Beretta, L. Patriarca, L. Rigoni, S. Foletti, Experimental and numerical investigation on compressive fatigue strength of lattice structures of AlSi7Mg manufactured by SLM, Int. J. Fatigue. (2019). doi:10.1016/j.ijfatigue.2019.06.041.

[70] R. Casati, M. Vedani, Aging Response of an A357 Al Alloy Processed by Selective Laser Melting, Adv. Eng. Mater. 0 (2018) 1800406. doi:10.1002/adem.201800406.

[71] I. Yadroitsev, P. Krakhmalev, I. Yadroitsava, S. Johansson, I. Smurov, Energy input effect on morphology and microstructure of selective laser melting single track from metallic powder, J. Mater. Process. Technol. 213 (2013). doi:10.1016/j.jmatprotec.2012.11.014.

[72] E. Louvis, P. Fox, C.J. Sutcliffe, Selective laser melting of aluminium components, J. Mater. Process. Technol. 211 (2011) 275–284. doi:10.1016/j.jmatprotec.2010.09.019.

[73] R. Leach, Characterisation of areal surface texture, 2013. doi:10.1007/978-3-642-36458-7.

[74] ASTM E2283 - 08(2014), Standard Practice for Extreme Value Analysis of Nonmetallic Inclusions in Steel and Other Microstructural Features, (2014). doi:10.1520/E2283-08R14.2.

[75] J.C.J. Newman, I.S. Raju, Stress-Intensity Factor Equations for Cracks in Three-Dimensional Finite Bodies Subjected to Tension and Bending Loads, in: S.N. Atluri (Ed.), Comput. Methods Mech. Fract., Elsevier Science Publishers, 1986: pp. 311–334.

[76] G.T. Smith, Surface texture: two-dimensional, in: G.T. Smith (Ed.), Ind. Metrol., Springer London, London, 2002: pp. 1–67. doi:10.1007/978-1-4471-3814-3_1.

[77] N.T. Aboulkhair, I. Maskery, C. Tuck, I. Ashcroft, N.M. Everitt, Improving the fatigue behaviour of a selectively laser melted aluminium alloy: Influence of heat treatment and surface quality, Mater. Des. 104 (2016) 174–182. doi:10.1016/j.matdes.2016.05.041.

[78] J.-P. Kruth, G. Levy, F. Klocke, T.H.C. Childs, Consolidation phenomena in laser and powder-bed based layered manufacturing, CIRP Ann. - Manuf. Technol. 56 (2007) 730–759. doi:10.1016/j.cirp.2007.10.004.

[79] Y. Murakami, M. Endo, Effect of Hardness and Crack Geometries on DKth of Small Cracks Emanating from Small Defects, in: K.J. Miller, E.R. de los Rios (Eds.), Behav. Short Fatigue Cracks, EGF Pub. 1, Mechanical Engineering Publications, London, 1986: pp. 275–293.

[80] Y. Murakami, K. Takahashi, T. Yamashita, Quantitative Evaluation of The Effect of Surface Roughness, Trans. Japan Soc. Mech. Eng. Ser. A. 63 (1997) 12–19.

[81] C.M. Sonsino, H. Kaufmann, V. Grubisic, Übertragbarkeit von Werkstoffkennwerten am Beispiel eines betriebsfest auszulegenden geschmiedeten Nutzfahrzeug-Achsschenkels, Konstruktion. 47 (1995)

222–232.

[82] G. Härkegård, G. Halleraker, Assessment of methods for prediction of notch and size effects at the fatigue limit based on test data by Böhm and Magin, Int. J. Fatigue. 32 (2010) 1701–1709. doi:10.1016/j.ijfatigue.2010.03.011.

[83] R. Kuguel, A relation between theoretical stress concentration factor and fatigue notch factor deduced from the concept of highly stressed volume, in: Proc. ASTM, 1961: pp. 732–748.

[84] S. Romano, S. Miccoli, S. Beretta, Pro-FACE: a finite element-based post-processor for probabilistic fatigue assessment of AM parts, Int. J. Fatigue 125 (2019) 324-341.

[85] S. Beretta, Affidabilità delle costruzioni meccaniche, Springer, Milano, 2009. doi:10.1007/978-88-470-1079-6.